19

Characterization of Complex Materials by Scanning Tunneling Microscopy

A Look at Superconductors with High Critical Temperatures

Zhe Zhang and Charles M. Lieber*

Department of Chemistry and Division of Applied Sciences, Harvard University, Cambridge, MA 02138

Scanning tunneling microscopy (STM) is becoming an increasingly important tool for materials research because STM can provide direct, real-space information about the local structure and electronic properties of complex solids. In this chapter, we illustrate new and important information obtained from STM studies of copper oxide superconductors with high critical temperatures. As a prelude to the experimental results, the basic theoretical concepts needed to understand and interpret the STM experiment are discussed. Then, STM investigations of the normal and superconducting states of $Bi_2Sr_2CaCu_2O_8$ solids are reviewed. STM measurements were used to elucidate the nature of structural disorder in the BiO layer and the corresponding changes in the electronic states as a function of oxygen doping. In addition, studies of the superconducting state were used to illuminate the superconducting energy gap of $Bi_2Sr_2CaCu_2O_8$ and other low-temperature phenomena.

*Corresponding author

0065–2393/95/0245–0479$14.25/0

UNDERSTANDING THE ELECTRONIC AND STRUCTURAL PROPERTIES of materials from the knowledge of atomic- and molecular-level properties is a focus of current research efforts in solid-state chemistry. This understanding is essential to the materials sciences because it will lead the way to the rational design and preparation of new solids with predictable properties. Two new approaches that have begun to provide key atomic-level structural and electronic information are scanning tunneling microscopy (STM) and scanning tunneling spectroscopy (STS) (*1–7*). STM and STS can be used to directly image the atomic structures and electronic properties of the interfaces of conductors and semiconductors.

As a surface-sensitive technique, STM provides experimental information that may be of questionable value when used to provide insight into the bulk properties of materials. The surfaces of low-dimensional solids such as the transition metal dichalcogenides and the copper oxide superconductors often terminate with bulk structure and bonding. In these cases, STM was shown to provide key insight into the structure and electronic properties of the bulk (*7–17*).

The focus of this chapter is the applications of STM and STS to the elucidation of the complex structural and electronic properties of the copper oxide superconductor $Bi_2Sr_2CaCu_2O_8$ (*18, 19*). First, the basic experimental and theoretical concepts of STM will be reviewed. The remainder of the chapter will then concentrate on several experimental studies of the $Bi_2Sr_2CaCu_2O_8$ system, including (1) the atomic-level nature of structural disorder in the BiO layer of $Bi_2Sr_2CaCu_2O_8$ and the low-energy electronic states associated with this structure, (2) the structural and electronic consequences of oxygen doping of $Bi_2Sr_2CaCu_2O_8$, and (3) low-temperature STS studies of the $Bi_2Sr_2CaCu_2O_8$ superconducting energy gap.

An Introduction to STM and Tunneling

In this section, we briefly review the instrumentation and theoretical concepts that are essential for understanding the STM studies that will be discussed. More detailed reviews can be found elsewhere (*4, 20–22*). A typical tunneling microscope is illustrated schematically in Figure 1. The underlying basis for the operation of the microscope is electron tunneling between a sharp metal tip and a conducting sample. When the tip and sample are sufficiently close, their wave functions can overlap. If a bias voltage, V, is then applied to the sample, a tunneling current, I, will flow between the sample and tip.

Electrons will tunnel from filled electronic states in the tip to empty states in the sample when V is positive; conversely, electrons will tunnel

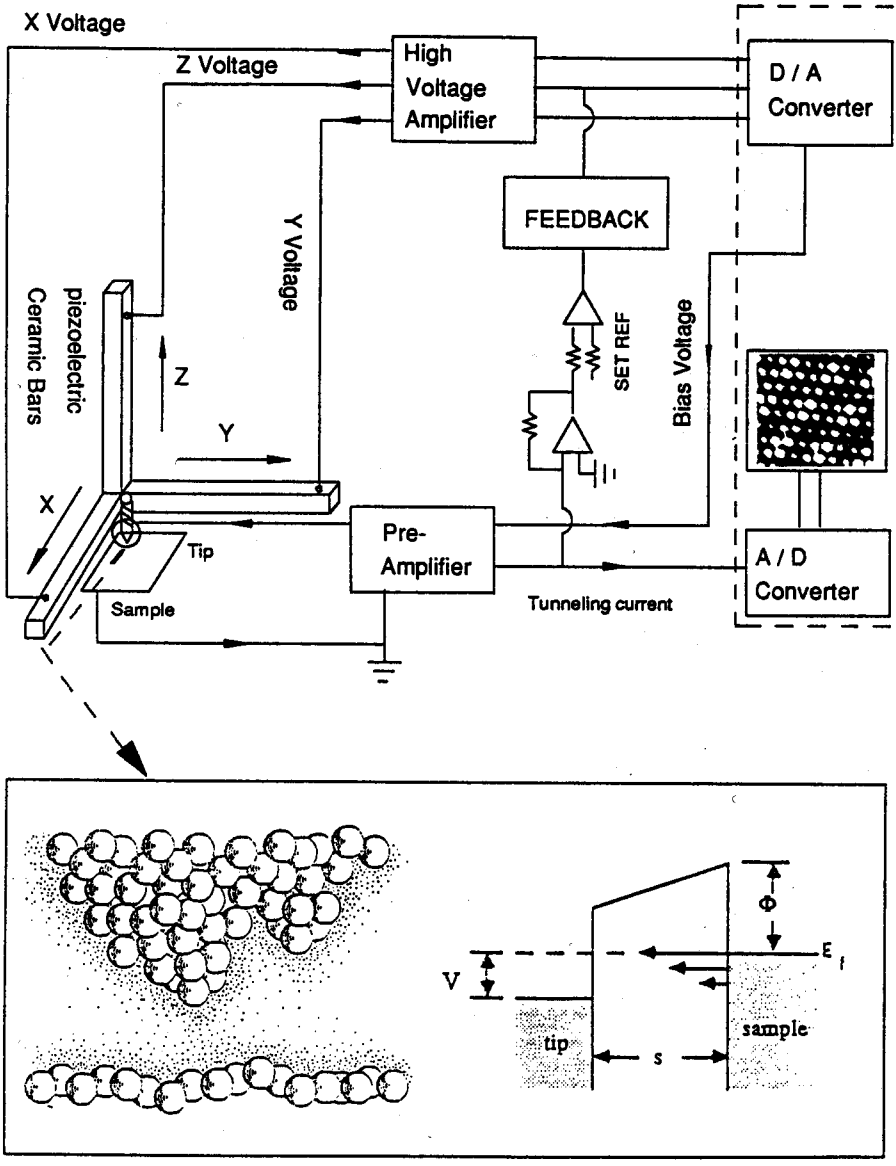

Figure 1. Schematic illustration of a tunneling microscope. The inset is a one-dimensional representation of tunneling between a metallic sample and tip, where s *is the tip–sample separation,* V *is the applied voltage,* E_f *is the Fermi energy, and* ϕ *is the average work function.*

from filled sample states to empty tip states when V is negative (Figure 1). The tunneling current that flows when V is applied varies exponentially with the tip–sample separation. For a typical work function of 4 eV, I decreases 10-fold for a 1-Å increase in separation. The actual decay rate can, however, vary significantly with the barrier properties. The strong exponential dependence of the tunneling current on distance enables STM to achieve high vertical resolution. An atomic resolution map of the surface can then be generated by rastering the tip over the sample with angstrom-level control by using piezoceramic positioners. Experimental images are typically acquired in the constant-current mode in which a feedback loop controls the vertical position of the tip above the sample so that I is equal to a reference current (I_{ref}) at all coordinates on the surface. Therefore, features in constant-current-mode images correspond to vertical displacements of the piezoceramic positioner needed to maintain a constant tunneling current.

An understanding of the response of the tunneling current to the barrier properties, applied voltage, and so on, is essential to the interpretation of such STM data; insight into these problems can be obtained from theoretical analyses of the tunneling problem (*23–28*). As first discussed by Tersoff and Hamann (*23, 24*), an expression for I can be derived readily by assuming unperturbed sample and tip wave functions and then by using perturbation theory. In the limit of small bias voltage and low temperature, this treatment yields

$$I = (2\pi/\hbar)e^2V \sum |M_{st}|^2 \delta(E_s - E_f)\delta(E_t - E_f) \qquad (1)$$

where M_{st} is the tunneling matrix element between wave functions on the tip, ψ_t, and sample, ψ_s; V is the bias voltage; $\hbar$ is Planck's constant; δ is the delta function; and E_s, E_t, and E_f are the sample, tip, and Fermi energies, respectively. As shown by Bardeen (*29*), the tunneling matrix can be written

$$M_{st} = (\hbar^2/2m) \int (\psi_t^* \nabla \psi_s - \psi_s \nabla \psi_t^*) dS \qquad (2)$$

where m is the mass of the electron; ∇ is the differential operator; and the integral corresponds to a surface, S, within the barrier region between the sample and tip. To evaluate M_{st} in a way that the resulting expression for I can be compared quantitatively to STM images in general (i.e., not for one specific choice of sample and tip) requires several approximations. Tersoff and Hamann (*23, 24*) showed that by assuming the tip forms a

locally spherical potential well with only s-wave functions, I could be expressed as

$$I \propto \sum_s | \psi_s(r_o) |^2 \delta(E_s - E_f) \tag{3}$$

where r_o is the center of curvature of the tip. By definition, the summation is the local density of sample electronic states, $\rho(r_o,E)$, at the center of curvature of the tip

$$\rho(r_o,E) \equiv \sum_s | \psi_s(r_o) |^2 \delta(E_s - E_f) \tag{4}$$

and thus, constant-current images correspond to contours of constant density of sample electronic states.

In view of the simplicity of this result, the effect of the approximations made in deriving equation 4 are considered. Treatment of the tip as a spherical potential is reasonable because in almost all cases the experimental tip shape is unknown, although it probably terminates in a cluster of atoms; that is, the tip is approximately spherical. The s-wave function approximation for the tip is more significant because it leads to a cancellation in equation 2 such that I depends only on the square of the sample wave function. Recently, Tersoff (*27*) examined more general descriptions of the tip and found that for metals, constant-current images still correspond to contours of constant density of sample electronic states. STM images of semiconductor surfaces at low V could, however, deviate significantly from this simple picture because only a small pocket of the surface Brillouin zone contributes to the tunneling. This deviation is limited, however, to the lowest Fourier component of the image, and the model of the s-wave function tip may still be used in many cases to interpret images.

In contrast, Chen (*28*) suggested that the s-wave function approximation is unable to explain the resolution obtained in many experiments and that the tip function should be taken as a p_z or d_{z^2} dangling-bond state. Using this tip model, Chen was able to consistently explain atomic resolution images of close-packed metal surfaces. Although these results indicate that significant progress has been made in understanding the role of the tip, future development of these theoretical models is important so that experimental data can be quantitatively interpreted.

In the foregoing discussion, we showed that for reasonable approximations, constant-current STM images correspond to contours of constant local density of sample electronic states. We now examine the tunneling

current expression further to determine the explicit dependence of I on tip–sample separation and V. First, if we account for the exponential decay of the sample and tip wave functions into the tunneling gap, we can rewrite equation 3 as

$$I \propto \sum_s |\psi_s|^2 \exp[-2\kappa(R + s)]\delta(E_s - E_f) \quad (5)$$

where R is the radius of the tip, and s is the tip–sample separation. The decay parameter, κ, can be written as

$$\kappa = [(2m\phi/\hbar^2) + k^2]^{1/2} \quad (6)$$

where ϕ is the average work function, and k is the parallel wave vector component of ψ_s (*30*). For tunneling between planar, free-electron, metal electrodes at small bias (i.e., $V << \phi$), equation 5 can be written as

$$I \propto (V/s) \exp(-2\kappa s) \quad (7)$$

with $\kappa = 1.025\sqrt{\phi}$ (*30*). If we consider only the dominant exponential part of equation 7, we can express the work function as

$$\phi = 0.952(\mathrm{d} \ln I / \mathrm{d}s)^2 \quad (8)$$

Equation 8 indicates that the work function can be determined by measuring the distance dependence of the tunneling current; however, the derivation of equation 8 does not consider modifications of the barrier due to the close proximity of the two electrodes (i.e., the STM tip and sample). Lang (*31*) demonstrated that the slow decay of the exchange correlation potential causes the apparent work function to be less than the true sample work function for electrode separations appropriate to the STM experiment. Hence, the barrier height measured by STM is generally smaller than the sample work function.

In addition, we consider tunneling simultaneously from two distinct layers in a solid, such as the BiO and CuO layers of $Bi_2Sr_2CaCu_2O_8$. If we assume that the work functions of layers 1 and 2 are the same, then the ratio of the tunneling currents, I_1/I_2, from these layers is

$$I_1/I_2 = \exp\left[-1.025\sqrt{\phi}(s_2 - s_1)\right] \quad (9)$$

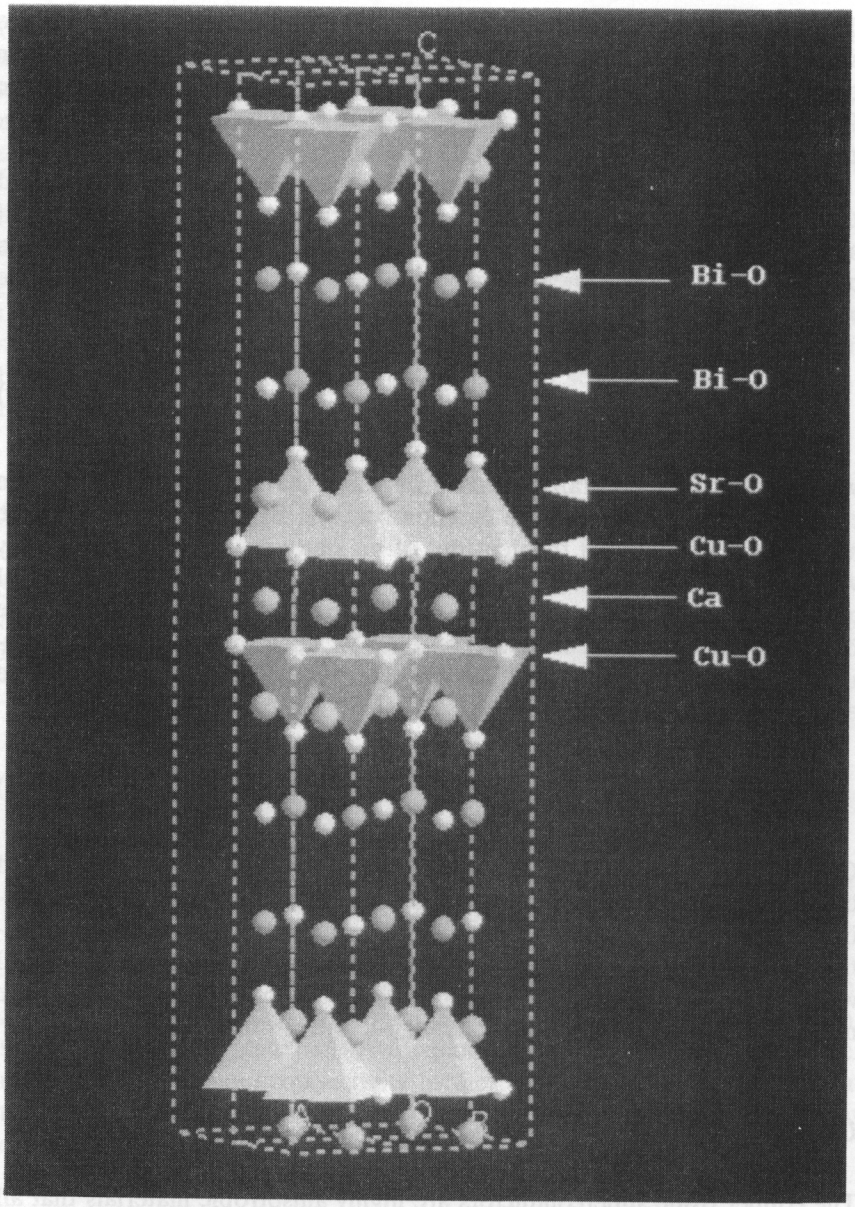

Figure 2. Structural view of $Bi_2Sr_2CaCu_2O_8$ highlighting the quasi-two-dimensional nature of this solid. Crystals cleave preferentially between the Bi–O double layers in the structure (a–b plane); the Cu–O planes correspond to the bases of the square-pyramid polyhedra and are separated by Ca^{2+} ions. The metals are gray and the oxygen ions are white The c-axis is vertical with respect to the page in this model.

The average structure of $Bi_2Sr_2CaCu_2O_8$ obtained from diffraction studies is quite straightforward, although in reality these materials exhibit a wide range of structural complexities that are not yet well-characterized. For example, $Bi_2Sr_2CaCu_2O_8$ shows considerable disorder in the BiO layer's atomic structure, oxygen nonstoichiometry, and substitution of metals between the idealized layers shown in Figure 2 (*33–40*). The detailed nature of such local disorder is intrinsically difficult to address by conventional diffraction techniques, as are the electronic consequences of these structural variations. A complete picture of the microscopic properties of these materials is, however, almost certainly necessary to understand high-temperature superconductivity, because the structural disorder has a dimensionality similar to the superconducting-pair coherence length. To characterize the structure and low-energy electronic states of $Bi_2Sr_2CaCu_2O_8$ in detail, we have been using STM, and in the next section we summarize the status of our work on this system.

The BiO Layer of $Bi_2Sr_2CaCu_2O_8$. The crystallographic separation between adjacent BiO layers in $Bi_2Sr_2CaCu_2O_8$ is quite large, >3 Å, and as such provides a natural cleavage plane in crystals of this solid (*36, 37*). Because covalent bonds are not broken when crystals are cleaved between the weakly interacting BiO layers, the BiO surface layer does not reconstruct; therefore, the STM experiment probes properties similar to those found in the bulk (*41, 42*).

A large-area, gray-scale image of this freshly cleaved BiO layer of $Bi_2Sr_2CaCu_2O_8$ (critical temperature, T_c, = 85 K) crystal is shown in Figure 3. This image exhibits a one-dimensional superstructure with an average modulation of 27 Å along the *a*-axis. Images acquired simultaneously with positive (empty sample electronic states) and negative (filled sample states) bias voltages show the same features. These bias, voltage-dependent images demonstrate that the observed superstructure approximates the variation in the total DOS; hence, we can conclude that this modulation is a structural feature. Bulk X-ray and electron diffraction studies (*36–40*) show a similar modulation and support this conclusion. The following models were proposed to explain the origin of this unique structural modulation in $Bi_2Sr_2CaCu_2O_8$: (1) lattice mismatch between the BiO and CuO layers, (2) extra oxygen substituted into the BiO layer that causes it to periodically buckle, and (3) periodic Cu or Sr substitution for Bi in the BiO layer (*36–40*). At least three problems intrinsic to these materials have hampered diffraction-based efforts to elucidate the origin of this structure. First, the superstructure period is incommensurate with respect to the lattice; second, the BiO layer has considerable disorder; and third, the X-ray and electron-scattering cross sections for oxygen are significantly smaller than those for Bi.

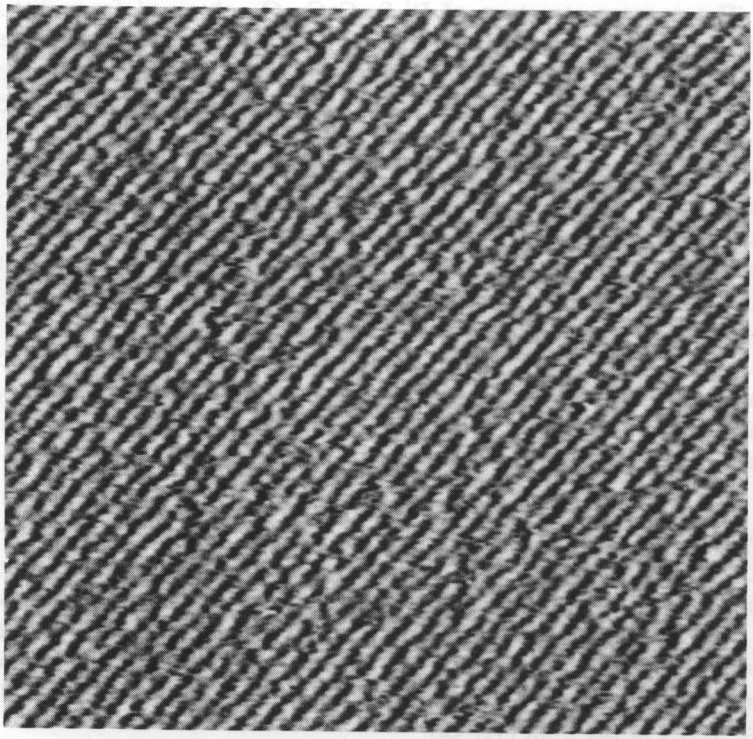

Figure 3. Image measuring 1000 × 1000 Å^2 of $Bi_2Sr_2CaCu_2O_8$ recorded with a bias voltage of 690 mV and a tunneling current of 0.8 nA.

STM is not limited by these problems and can, therefore, provide unique insight into the origin and effects of this modulation (*41–45*). For example, analyses of real-space STM images such as Figure 3 show that the superstructure period is not a sinusoidal modulation. The period varies from 22 to 27 Å, and the distribution of periods about the average is broad and non-Gaussian (*42*). These results strongly indicate that the superstructure is not due to simply BiO–CuO lattice mismatch (which would yield a sinusoidal modulation), but must have some substitutional component that causes local fluctuations in the superstructure period. Further evidence for the importance of substitution in determining the properties of the superstructure will be discussed in the context of our studies of oxygen doping in this system.

The large area images clearly indicate that substitution must play a role in the one-dimensional superstructure. In principle, atomically resolved images of the BiO lattice sites should resolve, in detail, the substitutional contribution to the modulation. A typical high-resolution image is shown in Figure 4. The atomic structure in this image has tetragonal

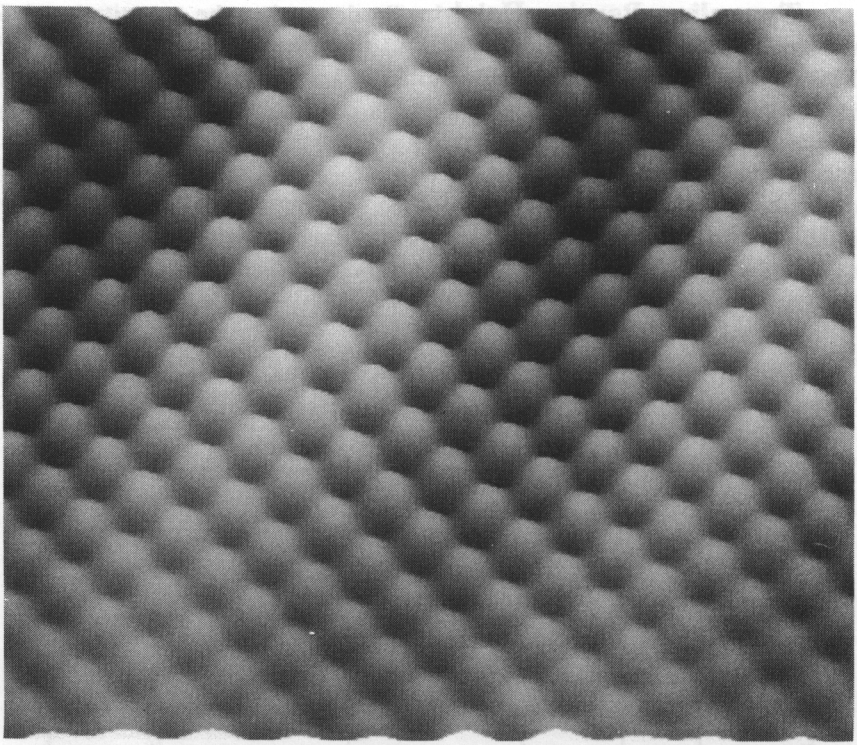

Figure 4. Atomic resolution image measuring 50 × 50 Å^2 of $Bi_2Sr_2CaCu_2O_8$ recorded with a bias voltage of 300 mV and a tunneling current of 1.4 nA.

symmetry with a period of 3.8 Å. This distance is consistent with both the average Bi–Bi and O–O distances determined by crystallography; that is, alternate atomic sites, either Bi or O, are imaged by STM. Because only one site is imaged by STM, these data cannot be used to unambiguously define the complete atomic structure associated with the superstructure modulation. The atomic resolution images do show, however, that significant positional disorder can exist in the BiO layer, and we believe this disorder reflects inhomogeneous substitution in the BiO layer. The atomic-scale disorder can be reduced by careful crystal-growth procedures.

The observation of alternate atomic sites indicates that the DOS are peaked over only one of the lattice sites, and hence, that the BiO layer may be semiconducting. STS is used to directly characterize the electronic character of the BiO layer. For finite bias-voltage spectroscopic measurements, our interpretation of the STS data is based on eqs 10 and 11. Applying this analysis [i.e., that $(V/I)dI/dV \propto$ LDOS)] requires that the tunneling barrier, ϕ, be greater than the bias voltage.

Tunneling Barrier Height. To determine the magnitude of ϕ, we characterized the dependence of I on tip–sample separation and on V. From the section "An Introduction to STM and Tunneling", we know that in the limit of free electron metals and small bias voltage, $I \propto \exp(-2\kappa s)$, where $\kappa = 1.025\sqrt{\phi}$. Hence, ϕ can be determined by measuring the distance dependence of the tunneling current. Figure 5 shows a typical I–s curve measured on $Bi_2Sr_2CaCu_2O_8$ taken at room temperature. The inset is ln (I)–s relationship. Analysis of these data yields a tunneling barrier of 2.6 eV; thus, the STS measurement should be confined between ±1.5 V for a meaningful interpretation.

Distance-Dependent Electronic States in $Bi_2Sr_2CaCu_2O_8$. To directly characterize the electronic character of the BiO layer, tunnel-

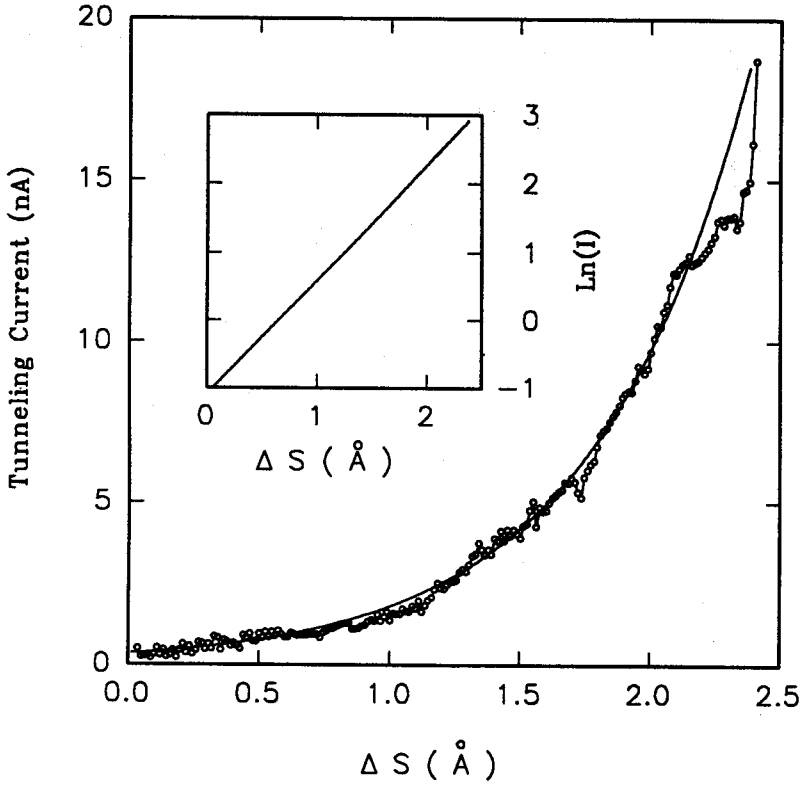

Figure 5. Current versus tip–sample separation measured for a typical as-grown sample. The tip was moved toward the surface after opening the feedback loop; the stabilized tunneling resistance was 10^9 Ω. The inset shows a plot of ln(I) versus distance. The apparent work function determined from these data is 2.6 eV.

ing spectroscopic measurements were performed (*42–45*). In contrast to other electronic spectroscopic methods, STM can provide a direct measure of the BiO layer electronic states and not a convolution of both BiO and CuO_2 layers. Such data are essential to the development of models of the electronic structure for this system. Current and normalized conductivity versus sample bias voltage curves obtained with a feedback-stabilized tunneling resistance of 10^9 Ω are shown in Figure 6. An important feature exhibited by these spectroscopic data is the apparent gap in the DOS at the Fermi level (E_f). Such data are reproducible on as-grown crystals (T_c = 85 K) and indicate that the BiO layer is semiconducting in these materials. In contrast, band-structure calculations using the full-potential, linearized, augmented, plane wave method suggested that the BiO layer is metallic (*46*), although these calculations do not consider the superstructure and other structural disorder present in the BiO layer. Interestingly, recent tight-binding calculations indicate that distortions in the BiO layer raise the energy of the Bi-derived band above E_f and drive the layer to a semiconducting state (*47*).

One striking phenomenon in this study is that the measured DOS change with the tip–sample separation (after correction for distance-dependent factors). In preliminary work, we found that STS measurements made at tip–sample separations closer than those used to record Figure 6 showed a finite DOS at E_f (*44*). More systematic measurements made in our group (*44*) and elsewhere (*45*) confirm this report (Figure 7). Specifically, when the tip is moved ~2 Å closer to the sample, the data show that the conductivity equals zero only at the origin. These results

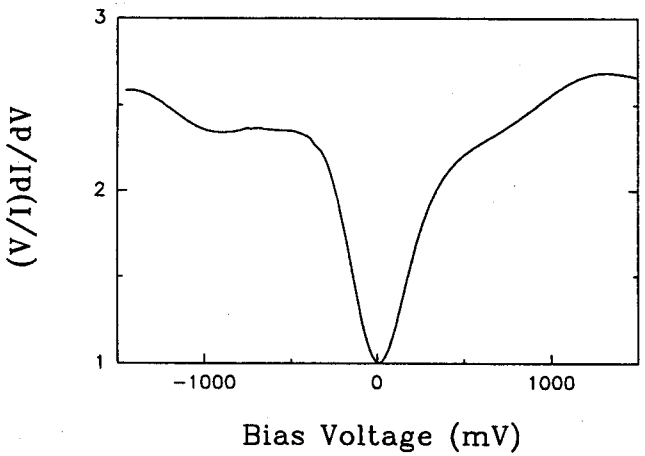

Figure 6. Plot of the normalized conductance versus sample bias voltage for $Bi_2Sr_2CaCu_2O_8$ sample. The voltage corresponds to the energy relative to E_f (V = 0).

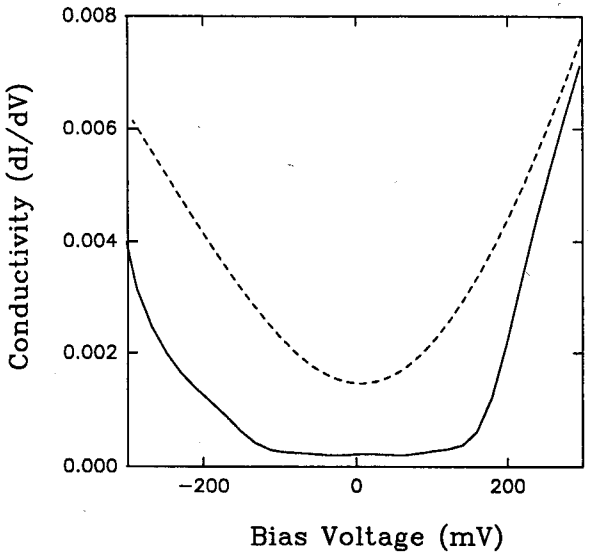

Figure 7. Conductance versus voltage curves recorded at two different tip–sample separations. The solid line was recorded with a tunneling resistance of 10^9 Ω, whereas the dashed line was measured with a tunneling resistance of 10^8 Ω.

demonstrate that for small tip–sample separations, no apparent gap in the DOS exists; that is, the BiO layer appears weakly metallic. One explanation that we (*44*) suggested for these observations is that the metallic states correspond to a tunneling contribution from the CuO layer that is 4.5 Å below the surface. Alternatively, the surface wave function may have an unusually short decay length (because k is >0). From the value of the apparent work function (2.6 eV) obtained from the section "An Introduction to STM and Tunneling", the decay length is not unusually short; therefore, we believe that this alternative hypothesis is unlikely.

Electronic and Structural Effects of Oxygen Doping. Oxygen doping plays a widely recognized, key role in determining the properties of copper oxide superconductors (*48–50*). For example, results from many studies established that variations in oxygen concentration (i.e., in $Bi_2Sr_2CaCu_2O_{8+\delta}$ where δ corresponds to a small change in oxygen stoichiometry) change the average carrier concentration and, thereby, T_c. Recent observations (*50*) also suggest that subtle oxygen rearrangements can lead to superconductivity and enhanced fractions of superconducting material even when the average oxygen stoichiometry remains constant. The physical properties depend not only on the absolute amount of oxygen, but also on the detailed arrangement of oxygen in the lattice. To

understand these and other important effects, variations in the microstructure and local electronic structure associated with oxygen doping must be characterized. Determination of the local structure, including oxygen positions by diffraction techniques, is inherently difficult because of crystal disorder and the small, scattering cross section of oxygen. In addition, spatial variations in the electronic properties due to oxygen doping will be especially important in determining superconductivity in short-coherence-length materials such as $Bi_2Sr_2CaCu_2O_{8+\delta}$, where δ is the change in oxygen concentration caused by doping.

To address this important problem, we used STM to characterize the local structural and electronic changes that occur in vacuum-annealed $Bi_2Sr_2CaCu_2O_{8+\delta}$ crystals (*51*). Oxygen was removed from as-grown superconducting crystals ($T_c \approx 85$ K) by vacuum annealing (pressure, P, $\approx 10^{-3}$ torr or 133 mPa) at 400 °C. We found that these conditions yield systematic decreases in T_c as a function of annealing time. The suppression of superconductivity through vacuum annealing is also reversible; that is, annealing nonsuperconducting crystals in air at 400 °C for more than 8 h yields $T_c \approx 85$ K superconducting material. Thermogravimetric analyses of our crystals show that these changes in T_c correspond to a reversible, 2.5–3.0% change in the oxygen concentration.

STM images recorded on nonsuperconducting samples from which ~3% oxygen was removed are shown in Figure 8. These images were recorded at 900 and 150 mV by switching the bias voltage on alternate scan lines; therefore, the two images are recorded in an identical spatial location on the sample surface. The image recorded at high V exhibits the one-dimensional superstructure characteristic of $Bi_2Sr_2CaCu_2O_8$. Notably, the superstructure period is unchanged in oxygen-deficient, nonsuperconducting samples compared with $Bi_2Sr_2CaCu_2O_8$. These results indicate that oxygen removed from the samples either does not come from the BiO layer or that oxygen loss from this layer has little effect on the superstructure. To address the structural location of oxygen loss more directly, we compared atomic resolution images of the BiO layer of nonsuperconducting and superconducting crystals (Figure 9) (*51*). Notably, images of the BiO layer of the oxygen-deficient crystals do not exhibit vacancies; therefore, oxygen might be lost from the SrO or CuO_2 layers. More studies are needed to resolve this important issue.

Images recorded at small V provide important additional information about the electronic effects of oxygen loss. Specifically, these data exhibit nonperiodic features in addition to a contribution from the one-dimensional superlattice. Analysis of images acquired over a range of V show that the superstructure has the same spatial location irrespective of V and represents a true structural feature. The fact that the irregular features are observed only for small V indicates that these features are due to variations in the electronic states near E_f. Because the low bias-voltage elec-

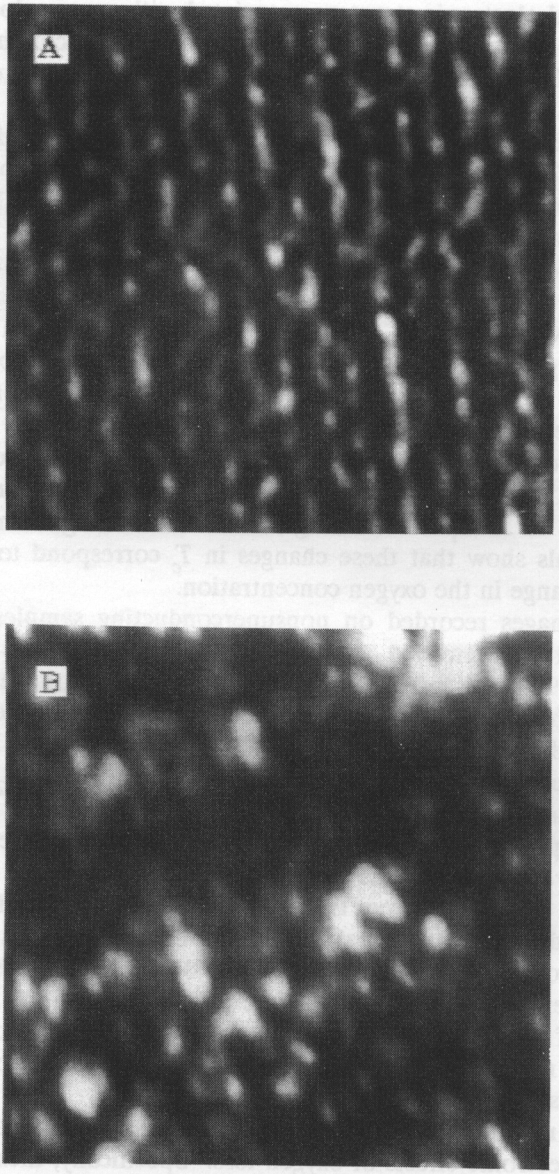

Figure 8. Image measuring 450 × 450 Å^2 of nonsuperconducting $Bi_2Sr_2CaCu_2O_8$ recorded with (A) V = 900 mV and (B) V = 150 mV. Adjacent maxima of the superstructure are separated by about 27 Å in A and B. Irregular electronic features are also detected at low bias in B.

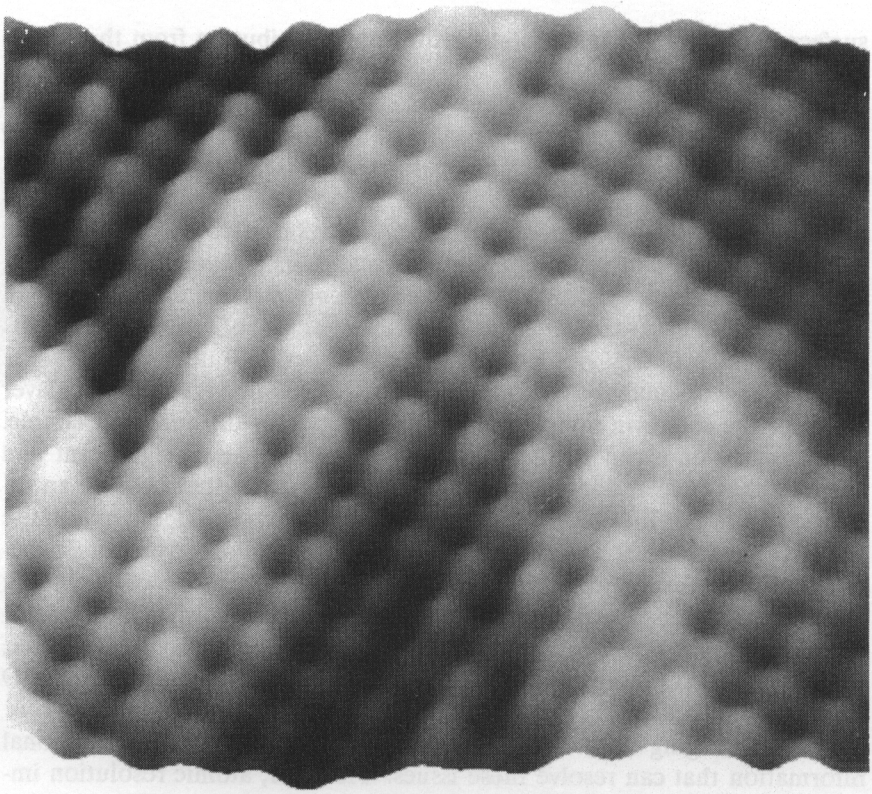

Figure 9. Image measuring 50 × 50 Å^2 of a nonsuperconducting sample recorded with a bias voltage of 360 mV and a tunneling current of 2 nA.

tronic states are not observed in images of superconducting samples, we conclude that they reflect spatial variations in the electronic properties due to oxygen loss. These electronic variations occur on the same scale as the coherence length (~20 Å) and may affect pairing in intermediate T_c crystals.

We also used STM and STS to characterize how the structure and electronic states evolve when additional oxygen is introduced into the lattice through high-pressure annealing (*52*). Recent X-ray photoemission spectroscopy studies of $Bi_2Sr_2CaCu_2O_{8+\delta}$ crystals doped in high-oxygen pressure show that the DOS of E_f increase with increasing δ (*53*). To explain this increase in the DOS, the suggestion was made that oxygen doping transformed the BiO structural element into a metallic layer (*53*). However, X-ray photoemission spectroscopy probes several unit cells in depth; therefore, these observed changes may or may not arise from variations in the BiO- or CuO_2-layer DOS. STM is uniquely suited to elucidate the origin of high-pressure doping because it can directly probe the

surface BiO-layer electronic states with little contribution from the underlying CuO_2 planes.

Spectroscopic data obtained on as-grown and oxygen-annealed $Bi_2Sr_2CaCu_2O_8$ crystals that were cleaved are shown in Figure 10. A key result that is immediately evident upon comparison of the data is the distinctly different I–V behavior near E_f for the as-grown and oxygen-annealed samples. The as-grown crystals exhibit a low current within ±200 mV of E_f and relatively sharp increases in I beyond these points, whereas the oxygen-annealed samples show a smooth increase in I for all V. Because the tip–sample separation is similar in both experiments, this difference is probably not due to a distance-scaling effect. Indeed, the normalized conductivity, $(V/I)dI/dV$, shows a 330-mV gap in BiO-layer DOS for the as-grown sample but no obvious gap for the annealed sample. The absence of a gap in the oxygen-annealed samples is significant and suggests that oxygen doping introduces impurity states that obscure an intrinsic gap in the BiO-layer DOS. Alternatively, oxygen doping may cause the BiO band to shift and cross E_f; in this case, the BiO layer will be metallic. STS measurements provide only a relative measure of the DOS; therefore, these two hypotheses are difficult to distinguish without additional experiments. Qualitatively, we (*54*) noted that the conductance, dI/dV, of the BiO layer appears to be lower than that of the metallic TlO layer of $Tl_2Ba_2CaCu_2O_8$ (Tl-2212) crystals.

STM imaging of the BiO layer's atomic structure provides additional information that can resolve these issues. However, atomic resolution images of the as-grown and oxygen-annealed samples show virtually identical surface structures (Figure 11). The lattices for both samples have periods of 3.8 ± 0.2 Å that correspond to either the Bi–Bi or O–O lattice sites. The observation of alternate lattice sites for a range of bias conditions indicates that the Bi–O layer is semiconducting in both as-grown and oxygen-annealed crystals. A recent STM study (*54*) of the related system Tl-2212 showed that simultaneous imaging of both Tl and O sites is possible when the surface is metallic; therefore, the present data probably did not result from an instrumental limitation. Most likely, the BiO-layer DOS near E_f increases with oxygen annealing but the layer remains semiconducting.

The mechanism of oxygen doping in the $Bi_2Sr_2CaCu_2O_8$ system is also important to consider. If the increase in the DOS were due to oxygen incorporated into the BiO layer, then we would expect either extra lattice sites or a locally distorted structure. Comparisons of the images of as-grown and oxygen-annealed samples do not exhibit evidence for such structural defects (Figure 11). These results suggest (but do not prove) that oxygen is not incorporated directly into the BiO layer of the annealed samples. Another explanation, which is consistent with our structural and electronic data, is that oxygen is incorporated into Cu–Bi vacancy or inter-

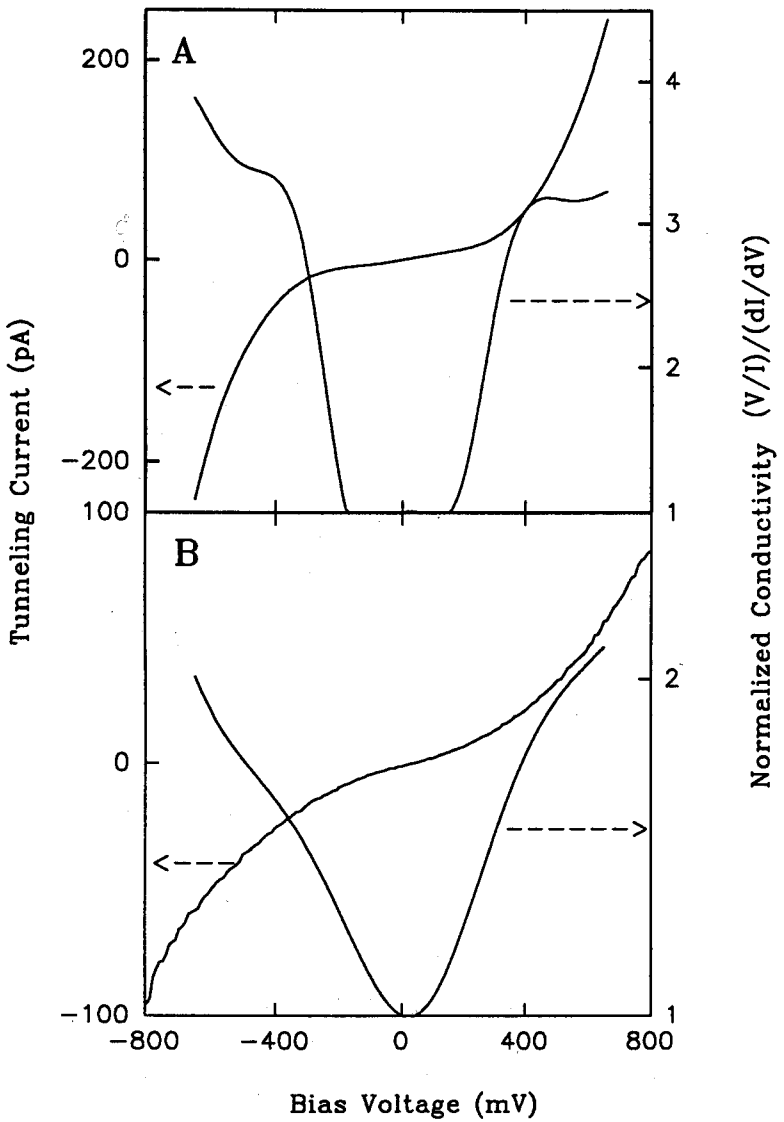

Figure 10. Typical I–V *data obtained on as-grown (A) and oxygen-annealed (B) samples. The feedback stabilized tunneling resistance,* 10^9 Ω, *was the same for both experiments. Normalized conductance curves,* (V/I)dI/dV, *corresponding to the as-grown and oxygen-annealed samples are also shown.*

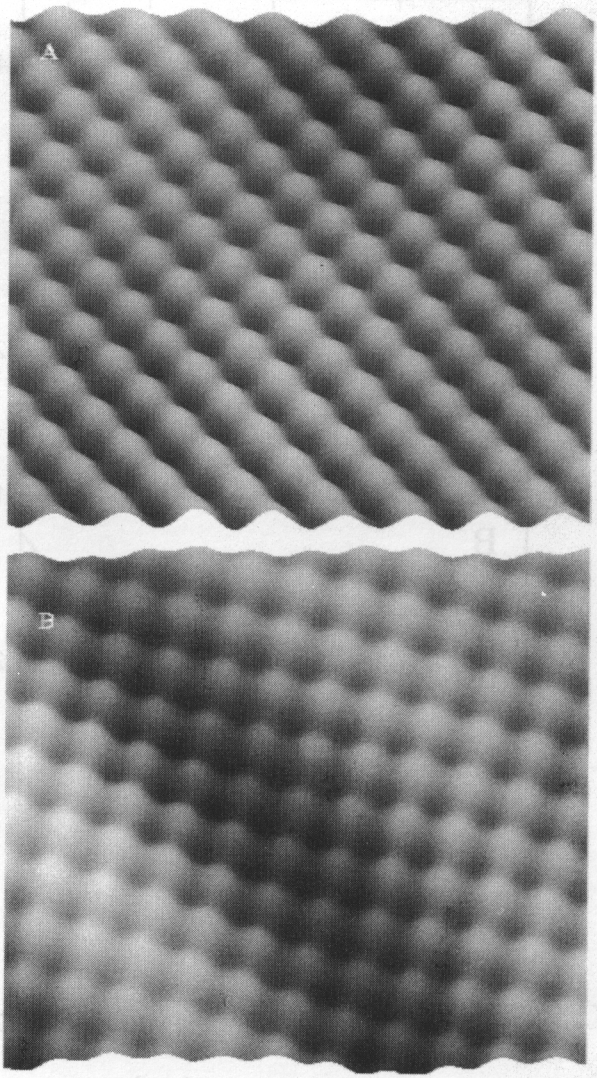

Figure 11. An STM image measuring 40 × 40 Å^2 recorded on (A) as-grown and (B) 12-atm, oxygen-annealed $Bi_2Sr_2CaCu_2O_8$ cleaved single crystals. The tetragonal lattice spacing in the two images is 3.8 Å. The images were recorded by using bias voltage and tunneling current, respectively, of (A) 300 mV and 0.9 nA, and (B) 250 mV and 1.8 nA.

stitial sites in the SrO layers. This oxygen would cause only subtle changes in the BiO layer structure and DOS, as observed in our experiments.

Studies of $Bi_2Sr_2CaCu_2O_8$ in the Superconducting State

A detailed picture of the energy gap (2Δ) and low-energy excitations is essential to understand the mechanism of superconductivity in the copper oxide materials. The Bardeen–Cooper–Schrieffer (BCS) theory of superconductivity predicts that a complete gap in the density of electronic states exists as T approaches zero, and that the magnitude of 2Δ has the universal value of $3.53kT_c$ (*55*). For conventional superconductors, these predictions have agreed well with measurements of the DOS by tunneling spectroscopy (*56*). For the copper oxide materials, however, tunneling spectroscopy measurements have led to suggested values of 2Δ between 0 and 12 kT_c, although recent studies (*57–67*) seem to converge toward an energy scale of 5–8 kT_c. Furthermore, large conductances within $\pm\Delta$, which suggest that a true energy gap may not exist, were reported by several groups (*58, 61–63*).

Material inhomogeneities such as oxygen nonstoichiometry probably have been responsible for many of the apparently conflicting measurements of 2Δ by tunneling spectroscopy (*63, 64, 67*). The short coherence lengths of the copper oxide materials make tunneling measurements especially susceptible to local variations in the superconducting properties. Hence, we (*67*) placed considerable effort on STS measurements of $Bi_2Sr_2CaCu_2O_{8+\delta}$ crystals that were carefully annealed to produce homogeneous samples. Our tunneling measurements were made in two distinct ways with low-temperature STM. First, we studied normal metal–insulator–superconductor (NIS) junctions formed between a Pt-tip and $Bi_2Sr_2CaCu_2O_{8+\delta}$ superconductor. These junctions provide a direct measure of 2Δ. Second, we investigated superconductor–insulator–superconductor (SIS) junctions formed between two pieces of $Bi_2Sr_2CaCu_2O_{8+\delta}$ material. These latter junctions provide a direct measure of 4Δ.

Typical I–V and dI/dV versus V curves obtained by using NIS junctions at 4.2 K are shown in Figure 12. These results are representative of several hundred data sets obtained on the annealed $Bi_2Sr_2CaCu_2O_{8+\delta}$ crystals. The tunnel–junction resistances in our experiments varied from 10^7 to 10^9 Ω; within this range, similar results were observed. However, the current exhibits a weak, nonexponential dependence on tip–sample separation. This weak dependence on tip–sample separation indicates that the tip touches the sample surface during these experiments. In this contact geometry, the tunneling measurements average both a–b and c directions (*68*).

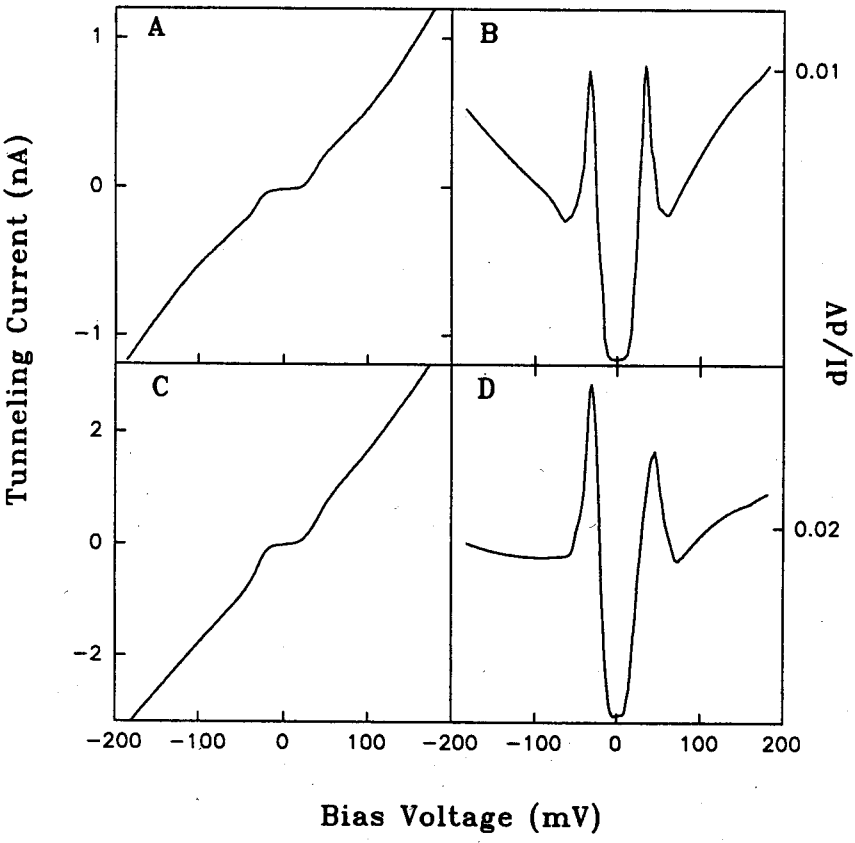

Figure 12. A and C: Typical I–V *curves obtained on oxygen-annealed* $Bi_2Sr_2CaCu_2O_8$ *single crystals at 4.2 K. These NIS junctions were formed between a Pt–Ir tip and cleaved* $Bi_2Sr_2CaCu_2O_8$ *crystal surfaces. B and D: Conductance (dI/dV) versus voltage curves corresponding to the* I–V *data in A and C, respectively. The curves exhibit well-developed gap structure and linear background conductance for* $|V| > \pm\Delta$. *Conductances at* $V = 0$ *in B and D are 8 and 5%, respectively, of G(100).*

Qualitatively, the *I–V* curves exhibit a flat, low-current region about the Fermi level (E_f, $V = 0$) and relatively sharp conductance onsets at ±25 mV. These features are characteristic of a conventional superconducting energy gap. Interestingly, this well-developed gap structure is observed reproducibly over the surfaces of oxygen-annealed $Bi_2Sr_2CaCu_2O_{8+\delta}$ samples. In contrast, we observe a wide range of *I–V* behavior on as-grown $Bi_2Sr_2CaCu_2O_{8+\delta}$ samples; these variations are similar to those found in other reports (*63*). Therefore, much of the uncertainty observed in previous work may be due to oxygen nonstoichiometry. In the following sec-

tion, we confine our analysis solely to reproducible measurements obtained on oxygen-annealed $Bi_2Sr_2CaCu_2O_{8+\delta}$ samples.

The conductance, $G(V) = dI/dV$, versus voltage curves provide essential insight into the nature of the superconducting gap in these materials (Figures 12C and 12D). The conductance within the gap is low. For the NIS junctions, $G(0)/G(150)$ values, where $G(150)$ is representative of the normal-state conductance, are between 2 and 8%. These values can be compared with conductances of 30–50% reported previously (*59, 62, 63*).

We do find, however, large conductances in tunneling measurements made on the as-grown $Bi_2Sr_2CaCu_2O_{8+\delta}$ crystals. Because extrinsic effects such as sample inhomogeneity were not accounted for in the previous tunneling studies, these previous data are not necessarily indicative of d-wave pairing or gapless superconductivity. In our carefully annealed samples, $G(V)$ is very low at $V = 0$; however, the behavior of $G(V)$ for $V > 0$ is also important to consider.

First, the increase in $G(V)$ within the gap is not proportional to $|V|$. A linear increase in $G(V)$ would be a clear signature for gapless superconductivity (*60*); therefore, our results may argue against this possibility. Comparing the conductance at $V = 0$ and $V = \Delta/2$ predicted for s-wave BCS gap with our data, we find that the increase in $G(V)$ at $V = \Delta/2$ is close to or slightly larger than the increase predicted by a thermally broadened (4.2 K) BCS-gap expression (*see* Figures 12C and 12D, respectively). These results indicate close analogy to a conventional BCS-like gap; however, the divergence at the gap edge differs from conventional behavior.

Similar results were also obtained from SIS junctions; representative I–V and $G(V)$ curves are shown in Figure 13. The I–V curves exhibit a flat, low-current region about $V = 0$ and pronounced conductance onsets at approximately ±50 mV. The near-zero current region about E_f detected in the SIS measurements is approximately 2 times larger than in the NIS data. This observation is consistent with the measurement of 2Δ and 4Δ in the NIS and SIS junctions, respectively, and indicates that other effects such as the Coulomb blockade do not contribute significantly to our data.

The $G(V)$ curves from the SIS junctions also exhibit low conductance at E_f (~4%). The background conductance within the gap increases more rapidly than does the background conductance found for the NIS junctions. The increase in conductance could be due to either poor junction quality or gapless superconductivity. Poor SIS junction quality is probably the major factor leading to the increase in $G(V)$ within the gap; however, we do not have sufficient experimental evidence at this time to resolve the observed differences in the gap excitations for the NIS and SIS junctions. Regardless of the origin of the excitations observed in the gap of these SIS junctions, these data confirm the magnitude of 2Δ for the oxygen-

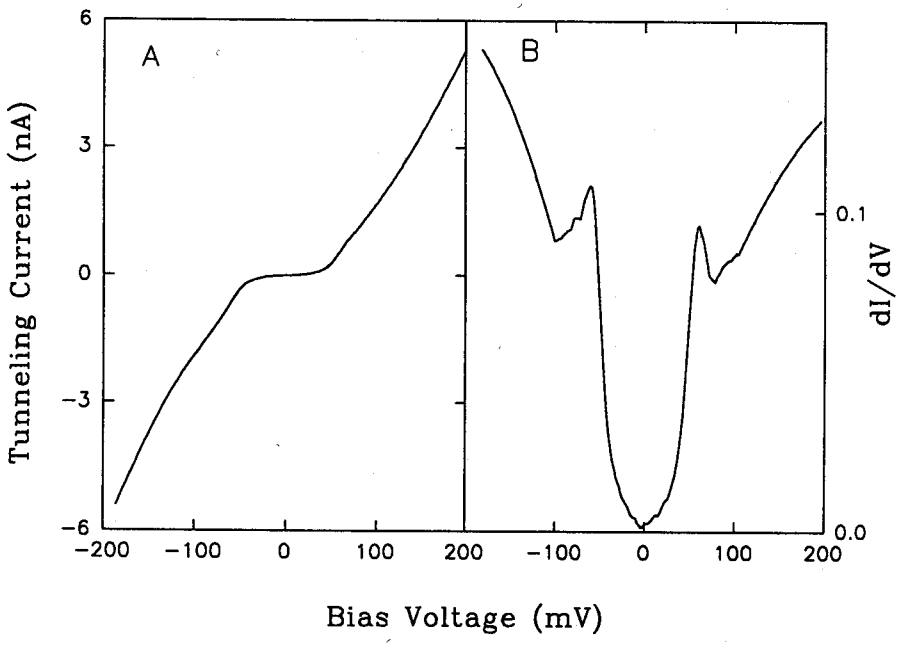

Figure 13. A: Representative I–V *curve obtained from an SIS junction formed between two oxygen-annealed* $Bi_2Sr_2CaCu_2O_8$ *crystals at 4.2 K. The junction geometry averages the* c *and* a–b *directions. B: Conductance versus voltage curve corresponding to the data in A. The conductance at* V = 0 *is 4% of* G(100). *The gap structure observed in the SIS junctions exhibits greater broadening than the data obtained from the NIS junction.*

annealed $Bi_2Sr_2CaCu_2O_{8+\delta}$ crystals and provide a consistent and reproducible energy scale for superconductivity.

In addition, we further analyzed the reproducible gap structure observed in our NIS measurements to quantitatively assign a value to 2Δ and to probe the energy dependence of the DOS. The experimental data were fit to the following modified BCS model for DOS:

$$N_S = R_e\{(eV - i\Gamma)/[(eV - i\Gamma)^2 - \Delta^2]^{1/2}\} \qquad (12)$$

where Γ is a phenomenological parameter to account for broadening, N_S is the density of states in the superconducting state, R_e corresponds to the real part of the complex number in braces {}, and i is $\sqrt{-1}$.

A typical fit using this model is shown in Figure 14. The experimental data are well-fit for $|V| < \Delta/2$, but the experimental conductance peaks are broadened significantly compared with the model DOS. Similar

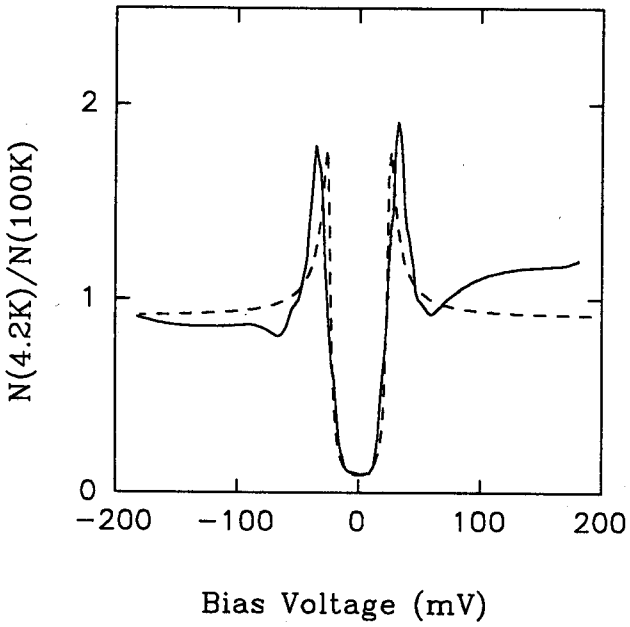

Figure 14. Conductance determined at 4.2 K normalized by the conductance at 100 K, G(4.2 K)/G(100 K), versus voltage for a typical NIS junction (solid line). The dashed line corresponds to a fit of this experimental data to the BCS model for DOS (see equation 12). This simple model for the superconducting state fits the gap structure well, although the experimental conductance peaks are significantly broader than the model fit. The values of Δ and Γ extracted from the model fit are 25 and 3 meV, respectively.

fits were also obtained for other $G(V)$ data with Γ = 1–3 meV; this broadening energy is greater than the thermal energy (0.36 meV). One should not, however, place too much significance on Γ because sample quality may still be limiting. That is, the finite transition widths indicate that the samples are not perfectly crystalline.

Nevertheless, this analysis has several different points. First, the well-defined gap in the NIS data can be fit at low energies by using a conventional model, although the broadening needed for a best-fit is greater than expected for only thermal effects. Second, the magnitudes of 2Δ and 4Δ extracted from our fits to the NIS and SIS data, 50 ± 5 and 98 ± 5 mV, respectively, show that the energy scale for superconductivity is $\sim 6.8kT_c$. The magnitude of 2Δ extracted from this analysis is, therefore, consistent with high-resolution, electron energy loss spectroscopic and photoemission spectroscopic measurements of $Bi_2Sr_2CaCu_2O_{8+\delta}$ crystals

(*66, 69, 70*). Lastly, the divergence in the experimental data at the gap edge is weak in comparison with the behavior expected for an s-wave BCS superconductor. This deviation from conventional behavior may be a signature of d-wave pairing or gapless superconductivity, although additional studies will be needed to confirm the intrinsic nature of the divergence.

These low-temperature STS studies of homogeneous, oxygen-annealed $Bi_2Sr_2CaCu_2O_{8+\delta}$ single crystals have shown that a well-developed gap structure can be observed reproducibly in high-quality samples. The low conductance and change of $G(V)$ observed within the gap region differ from the behavior expected for either a gapless or BCS-like superconductor and may indicate d-wave pairing. Analyses of data from both NIS and SIS junctions provide a consistent scale for superconductivity with $2\Delta \approx 6.8kT_c$.

Summary and Conclusions

STM and STS were used to characterize the electronic and structural properties of the high-temperature copper oxide superconductor $Bi_2Sr_2CaCu_2O_{8+\delta}$. In particular, these studies have done the following:

1. elucidated the local structural order in the BiO layer of $Bi_2Sr_2CaCuO_8$ and the low-energy electronic states associated with this disorder
2. characterized the structural and electronic effects caused by reducing and increasing the oxygen concentration in this material
3. determined a consistent value for the magnitude of the superconducting energy gap in $Bi_2Sr_2CaCuO_{8+\delta}$ single crystals

These data represent a firm beginning of a detailed microscopic picture of the structural and electronic properties for these complex materials. Continued STM and STS studies will undoubtedly lead to a much clearer understanding of superconductivity in the copper oxides. We believe that the use of STM and STS will also provide essential insight into many other problems in materials chemistry.

Acknowledgments

Charles M. Lieber thanks David and Lucile Packard of the National Science Foundation, Camille and Henry Dreyfus Foundation, and the A. P. Sloan Foundation for generous support of this work.

References

1. Binnig, G.; Rohrer, H.; Gerber, C.; Weibel, E. *Phys. Rev. Lett.* **1982,** *49,* 57.
2. Golovchenko, J. A. *Science (Washington, D.C.)* **1986,** *232,* 48.
3. Tromp, R. M.; Hamers, R. J.; Demuth, J. E. *Science (Washington, D.C.)* **1986,** *234,* 304.
4. Hamers, R. J. *Annu. Rev. Phys. Chem.* **1989,** *40,* 531.
5. Griffith, J. E.; Kochanski, G. P. *Annu. Rev. Mater. Sci.* **1990,** *20,* 194.
6. Avouris, P. *J. Phys. Chem.* **1990,** *94,* 2246.
7. Lieber, C. M.; Wu, X. L. *Acc. Chem. Res.* **1991,** *24,* 170.
8. Coleman, R. V.; Giambattista, B.; Hansma, P. K.; Johnson, A.; McNairy, W. W.; Slough, C. G. *Adv. Phys.* **1988,** *37,* 559.
9. Wu, X. L.; Lieber, C. M. *Science (Washington, D.C.)* **1989,** *243,* 1703.
10. Wu, X. L.; Lieber, C. M. *Phys. Rev. Lett.* **1990,** *64,* 1150.
11. Wu, X. L.; Lieber, C. M. *J. Am. Chem. Soc.* **1989,** *111,* 2731.
12. Chen, H.; Wu, X. L.; Lieber, C. M. *J. Am. Chem. Soc.* **1990,** *112,* 3326.
13. Wu, X. L.; Zhou, P.; Lieber, C. M. *Phys. Rev. Lett.* **1988,** *61,* 2604.
14. Wu, X. L.; Zhou, P.; Lieber, C. M. *Nature (London)* **1988,** *335,* 55.
15. Wu, X. L.; Lieber, C. M. *Phys. Rev. B.* **1990,** *41,* 1239.
16. Dai, H.; Chen, H.; Lieber, C. M. *Phys. Rev. Lett.* **1991,** *66,* 3183.
17. Wang, C.; Giambattista, B.; Slough, C. G.; Coleman, R. V. *Phys. Rev. B* **1990,** *42,* 8890.
18. Rao, C. N. R.; Raveau, B. *Acc. Chem. Res.* **1989,** *22,* 106.
19. Torardi, C. C.; Subramanian, M. A.; Calabrese, J. C.; Gopalakrishnan, J.; Morrissey, K. J.; Askew, T. R.; Flippen, R. B.; Chowdhry, U.; Sleight, A. W. *Science (Washington, D.C.)* **1988,** *240,* 631.
20. Hansma, P. K.; Tersoff, J. *J. Appl. Phys.* **1987,** *61,* R1. Hansma, P. K.; Elings, V. B.; Marti, O.; Bracker, C. E. *Science (Washington, D.C.)* **1988,** *242,* 209.
21. Kuk, Y.; Silverman, P. J. *Rev. Sci. Instrum.* **1989,** *60,* 165.
22. Sakurai, T.; Hashizume, T.; Kamiya, I.; Hasegawa, Y.; Sano, N.; Pickering, H. W.; Sakai, A. *Prog. Surf. Sci.* **1990,** *33,* 3.
23. Tersoff, J.; Hamann, D. R. *Phys. Rev. Lett.* **1983,** *50,* 1998.
24. Tersoff, J.; Hamann, D. R. *Phys. Rev. B* **1985,** *31,* 805.
25. Lang, N. D. *Phys. Rev. Lett.* **1986,** *56,* 1164.
26. Selloni, A.; Carnevalli, P.; Tosatti, P. E.; Chen, C. D. *Phys. Rev. B* **1986,** *33,* 5770.
27. Tersoff, J. *Phys. Rev. B* **1990,** *41,* 1235.
28. Chen, C. J. *Phys. Rev Lett.* **1990,** *65,* 448.
29. Bardeen, J. *Phys. Rev. Lett.* **1963,** *6,* 57.
30. Simmons, J. *J. Appl. Phys.* **1963,** *34,* 1793.
31. Lang, N. D. *Phys. Rev. B* **1988,** *37,* 10395.
32. Feenstra, R. M.; Stroscio, J. A.; Fein, A. P. *Surf. Sci.* **1987,** *181,* 295.
33. Whangbo, M.-H.; Torardi, C. C. *Acc. Chem. Res.* **1991,** *24,* 127.
34. Sleight, A. W. *Science (Washington, D.C.)* **1988,** *242,* 1539.
35. Ramakrishnan, T. V.; Rao, C. N. R. *J. Phys. Chem.* **1989,** *93,* 4414.
36. Subramanian, M. A.; Torardi, C. C.; Calabrese, J. C.; Gopalakrishnan, J.; Morrissey, K. J.; Askew, T. R.; Flippen, R. B.; Chowdhry, U.; Sleight, A. W. *Science (Washington, D.C.)* **1988,** *239,* 1015.

37. Gao, Y.; Lee, P.; Coppens, P.; Subramanian, M. A.; Sleight, A. W. *Science (Washington, D.C.)* **1988,** *241,* 954.
38. Zandbergen, H. W.; Groen, W. A.; Mijlhoff, F. C.; van Tendeloo, G.; Amelinckx, S. *Physica C (Amsterdam)* **1988,** *156,* 325.
39. Bordet, P.; Capponi, J. J.; Chaillout, C.; Chenavas, J.; Hewat, A. W.; Hewat, E. A.; Hodeau, J. L.; Marezio, M. *Stud. High Temp. Supercond.* **1989,** *2,* 171.
40. Eibl, O. *Physica C (Amsterdam)* **1991,** *175,* 419.
41. Kirk, M. D.; Nogami, J.; Baski, A. A.; Mitzi, D. B.; Kapitulnik, A.; Geballe, T. H.; Quate, C. F. *Science (Washington, D.C.)* **1988,** *242,* 1673.
42. Wu, X. L.; Zhang, Z.; Wang, Y. L.; Lieber, C. M. *Science (Washington, D.C.)* **1990,** *248,* 1211.
43. Tanaka, M.; Takahashi, T.; Katayama-Yoshida, H.; Yamazaki, S.; Fujinami, M.; Okabe, Y.; Mizutani, W.; Ono, M.; Kajimura, K. *Nature (London)* **1989,** *339,* 691.
44. Zhang, Z.; Wang, Y. L.; Wu, X. L.; Huang, J. L.; Lieber, C. M. *Phys. Rev. B* **1990,** *42,* 1082.
45. Shih, C. K.; Feenstra, R. M.; Chandrashekhar, G. V. *Phys. Rev. B* **1991,** *43,* 7913. Shih, C. K.; Feenstra, R. M.; Kirtley, J. R.; Chandrashekhar, G. V. *Phys. Rev. B* **1989,** *40,* 2682.
46. Massidda, S.; Yu, J.; Freeman, A. J.; Krakauer, H.; Pickett, W. E. *Phys. Rev. Lett.* **1988,** *60,* 1665.
47. Torardi, C. C.; Jung, D.; Kang, D. B.; Ren, J.; Whangbo, M.-H. *Mater. Res. Soc. Symp. Proc.* **1989,** *156,* 295.
48. Cava, R. J. *Science (Washington, D.C.)* **1990,** *247,* 656.
49. Daeumling, M.; Seuntjens, J. M.; Larbalestier, D. C. *Nature (London)* **1990,** *346,* 332.
50. Jorgensen, J. D.; Pei, S.; Lightfoot, P.; Shi, H.; Paulikas, A. P.; Veal, B. W. *Physica C (Amsterdam)* **1990,** *167,* 571.
51. Wu, X. L.; Wang, Y. L.; Zhang, Z; Lieber, C. M. *Phys. Rev. B* **1991,** *43,* 8729.
52. Zhang, Z.; Lieber, C. M. *Phys. Rev. B* **1992,** *46,* 5845.
53. Shen, Z.-X.; Dessau, D. S.; Wells, B. O.; Olson, C. G.; Mitzi, D. B.; Lombardo, L.; List, R. S.; Arko, A. J. *Phys. Rev. B* **1991,** *44,* 12098.
54. Zhang, Z.; Chen, C. C.; Lieber, C. M.; Morosin, B.; Venturini, E. L.; Ginley, D. S. *Phys. Rev. B* **1992,** *45,* 987.
55. Bardeen, J.; Cooper, L. N.; Schrieffer, J. R. *Phys. Rev.* **1957,** *108,* 1175.
56. Giaever, I. *Phys. Rev. Lett.* **1960,** *5,* 147.
57. Kirtley, J. R. *Int. J. Mod. Phys. B* **1990,** *4,* 201.
58. Hasegawa, T.; Ikuta, H.; Kitazawa, K. In *Physical Properties of High Temperature Superconductors III;* Ginsberg, D. M., Ed.; World Scientific Publishing: River Edge, NJ, 1992; p 525.
59. Valles, J. M.; Dynes, R. C.; Cucolo, A. M.; Gurvitch, M.; Schneemeyer, L. F.; Garno, J. P.; Waszczak, J. V. *Phys. Rev. B* **1991,** *44,* 11986.
60. Mandrus, D.; Forro, L.; Koller, D.; Mihaly, L. *Nature (London)* **1991,** *351,* 460.
61. Boekholt, M.; Hoffmann, M.; Guntherodt, G. *Physica C (Amsterdam)* **1991,** *175,* 127.

62. Huang, Q.; Zasadzinski, J. F.; Gray, K. E.; Liu, J. Z.; Claus, H. *Phys. Rev. B* **1989,** *40,* 9366.
63. Liu, J.-X.; Wan, J.-C.; Goldman, A. M.; Chang, Y. C.; Jiang, P. Z. *Phys. Rev. Lett.* **1991,** *67,* 2195.
64. Tao, H. J.; Chang, A.; Lu, F.; Wolf, E. L. *Phys. Rev. B* **1992,** *45,* 10622.
65. Chen Q.; Ng, K.-W. *Phys. Rev. B* **1992,** *45,* 2569.
66. Li, Y.; Huang, J. L.; Lieber, C. M. *Phys. Rev. Lett.* **1992,** *68,* 3240.
67. Zhang, Z.; Lieber, C. *Phys. Rev. B* **1993,** *47,* 3423.
68. Wolf, E. L. *Principles of Tunneling Spectroscopy;* Oxford University Press: New York, 1989.
69. Olson, C. G.; Liu, R.; Yang, A.-B.; Lynch, D. W.; Arko, A. J.; List, R. S.; Veal, B. W.; Chang, Y. C.; Jiang, P. Z.; Paulikas, A. P. *Science (Washington, D.C.)* **1989,** *245,* 731.
70. Dessau, D. S.; Wells, B. O.; Shen, Z.-X.; Spicer, W. E.; Arko, A. J.; List, R. S.; Mitzi, D. B.; Kapitulnik, A. *Phys. Rev. Lett.* **1991,** *66,* 2160.

RECEIVED for review November 9, 1992. ACCEPTED revised manuscript April 8, 1993.

Reprinted from ACS Advances in Chemistry Series No. 245
Materials Chemistry: An Emerging Discipline
Leonard V. Interrante, Lawrence A. Casper and Author B. Ellis, Editors